

# In Situ High Temperature Synthesis of Single-Component Metallic Nanoparticles

Yonggang Yao,<sup>†,‡</sup> Fengjuan Chen,<sup>†,‡</sup> Anmin Nie,<sup>§,¶</sup> Steven D. Lacey,<sup>†</sup> Rohit Jiji Jacob,<sup>||</sup> Shaomao Xu,<sup>†</sup> Zhennan Huang,<sup>⊥</sup> Kun Fu,<sup>†</sup> Jiaqi Dai,<sup>†</sup> Lourdes Salamanca-Riba,<sup>†</sup> Michael R. Zachariah,<sup>||,¶</sup> Reza Shahbazian-Yassar,<sup>⊥,¶</sup> and Liangbing Hu<sup>\*,†,¶</sup>

<sup>†</sup>Department of Materials Science and Engineering, University of Maryland, College Park, Maryland 20742, United States

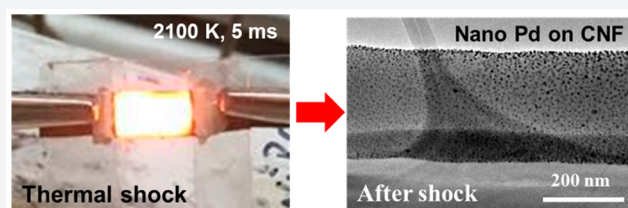
<sup>§</sup>Materials Genome Institute, Shanghai University, Shanghai 200444, China

<sup>||</sup>Department of Chemical Engineering and Chemistry, University of Maryland, College Park, Maryland 20742, United States

<sup>⊥</sup>Department of Mechanical and Industrial Engineering, University of Illinois at Chicago, Chicago, Illinois 60607, United States

## Supporting Information

**ABSTRACT:** Nanoparticles (NPs) dispersed within a conductive host are essential for a range of applications including electrochemical energy storage, catalysis, and energetic devices. However, manufacturing high quality NPs in an efficient manner remains a challenge, especially due to agglomeration during assembly processes. Here we report a rapid thermal shock method to *in situ* synthesize well-dispersed NPs on a conductive fiber matrix using metal precursor salts. The temperature of the carbon nanofibers (CNFs) coated with metal salts was ramped from room temperature to  $\sim 2000$  K in 5 ms, which corresponds to a rate of 400,000 K/s. Metal salts decompose rapidly at such high temperatures and nucleate into metallic nanoparticles during the rapid cooling step (cooling rate of  $\sim 100,000$  K/s). The high temperature duration plays a critical role in the size and distribution of the nanoparticles: the faster the process is, the smaller the nanoparticles are, and the narrower the size distribution is. We also demonstrated that the peak temperature of thermal shock can reach  $\sim 3000$  K, much higher than the decomposition temperature of many salts, which ensures the possibility of synthesizing various types of nanoparticles. This universal, *in situ*, high temperature thermal shock method offers considerable potential for the bulk synthesis of unagglomerated nanoparticles stabilized within a matrix.



## INTRODUCTION

Well-dispersed functional nanoparticles (NPs) in a conductive carbon host are particularly important for electrochemical energy storage, electrochemical catalysis, and photocatalysis, among other applications.<sup>1–6</sup> The conductive support can not only effectively transport electrons and heat generated during electrochemical reactions, but also disperse the nanoparticles from severe aggregation.<sup>7</sup> To date, two main strategies have been developed for the synthesis of NPs decorated on carbon-based materials: (1) synthesis-then-assembly<sup>5,8–10</sup> and (2) *in situ* growth.<sup>11–16</sup> For synthesis-then-assembly methods, a suspension of synthesized nanoparticles are introduced to the porous carbon matrix by impregnation and then drying. Such approaches allow for precise control of the NPs' size, phases, and structures by wet chemistry synthesis, and then the synthesized NPs are redispersed onto support.<sup>17–20</sup> Dispersion agents are usually required to stabilize the nanoparticle solutions, which can leave a residue on the nanoparticle surface and may deteriorate performance.<sup>14,21–24</sup> More often the NPs are prepared *in situ* on a carbon support via chemical reduction or hydrothermal reaction as a simple and low-cost method,<sup>11–16</sup> and sometimes via physical methods, such as electron beam radiation<sup>25–27</sup> and selective surface functionalization.<sup>28</sup>

Since carbon is nonwetting with most metals and the interaction between metal NPs and carbon surface is weak,<sup>29</sup> the as-formed nanoparticles are prone to agglomerate and redistribute during the synthesis and post heat treatments.<sup>16,24,30–33</sup>

As the growth and aggregation of nanoparticles are time dependent diffusion and migration processes, it is critical to synthesize ultrafine NPs over a short time and quench the process to prevent or, at least, minimize agglomeration. While conventional high temperature synthesis methods, such as spray pyrolysis and combustion, are fast (several seconds to minutes), a well controllable heating method is desirable for the control of both the high temperature heating process and also the resultant particle size and distribution.<sup>34–36</sup>

Here we report a one-step thermal shock method for rapid, *in situ* and surfactant-free synthesis of well-dispersed nanoparticles on a carbon matrix. Ultrafast thermal decomposition (400,000 K/s ramp rate) of metal salts on a carbon support was achieved by electrical Joule heating for 5 ms at high temperature ( $\sim 2000$  K). Palladium (Pd) nanoparticles acted

Received: December 6, 2016

Published: April 13, 2017

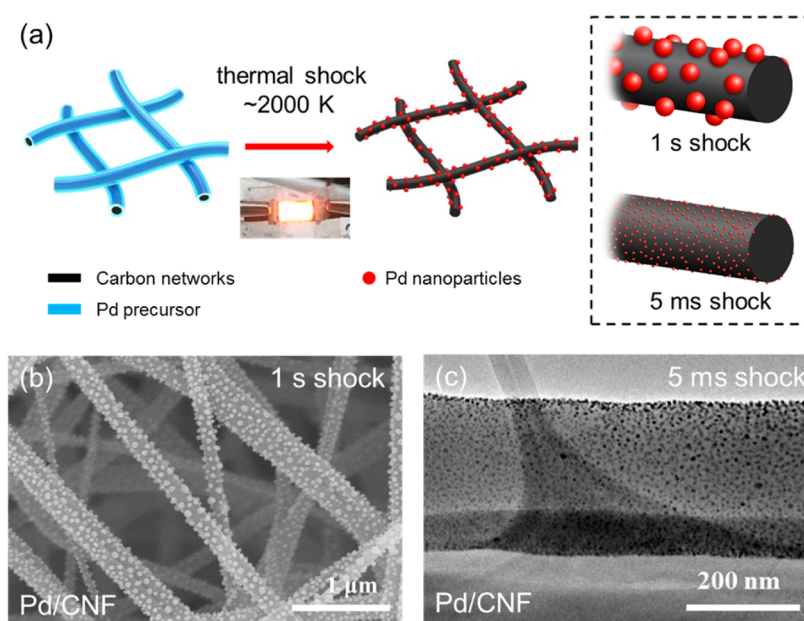


**Figure 1.** Synthesis of Pd NPs on CNFs via a rapid, high temperature thermal shock method. (a) Schematic to show the Pd NP formation process. Metal salt precursor  $\text{PdCl}_2$  is formed on the pristine CNF surface by a dip-coating method and then treated with a rapid thermal shock by Joule heating, which results in Pd NPs loading the carbon matrix. By utilizing different shock times, the NP size can be tuned: a faster shock creates smaller particle sizes. (b) SEM image of Pd/CNF formed by a 1 s thermal shock. (c) TEM image of Pd/CNF formed by a 5 ms thermal shock.

as the model system, however, gold (Au), iron (Fe), and tin (Sn) were also demonstrated using the proposed universal synthesis method. Due to a short thermal shock duration followed by ultrafast cooling, the metal atoms have limited time for migration, resulting in uniformly distributed NPs on the carbon support. In addition, the size distribution of the NPs strongly depends on the thermal shock duration; namely, a faster thermal shock process yields smaller nanoparticles with a more uniform size distribution. Compared to other synthesis methods for assembling nanoparticles on a carbon matrix, the proposed thermal shock process is facile and ultrafast and yields high purity and evenly distributed nanoparticles. By electrical Joule heating, the temperature can reach  $\sim 3000$  K, which enables the decomposition of most metal salts. Thus, a range of nanoparticles can be readily fabricated on carbon-based materials using this universal and ultrafast thermal shock method.

## RESULTS AND DISCUSSION

Figure 1a is a schematic representation of the proposed high temperature thermal shock method where NPs are rapidly assembled onto carbon nanofibers (CNFs). Pd nanoparticles were chosen as the model system to investigate the process–structure relationship in the proposed synthesis method. The pristine CNFs were dipped in an aqueous solution of  $\text{PdCl}_2$  (1 mg/mL) and dried in an oven to prepare  $\text{PdCl}_2$ -coated CNFs for the rapid thermal shock process. The rapid thermal shock was triggered by Joule heating, where the thermal energy can be easily controlled by the applied current. In a typical process, CNF- $\text{PdCl}_2$  was heated to  $\sim 2000$  K for 5 ms and cooled down immediately. The high temperature in the thermal shock process leads to the *in situ* thermal decomposition of  $\text{PdCl}_2$  at  $590$ – $740$  °C and the formation of Pd nanoparticles on the CNFs; the short shock time limits the diffusion and migration of the as-formed Pd nanoparticles and enables a uniform NP distribution across the CNFs. Note that CNFs were chosen as a

suitable carbon matrix due to its open network structure for gas releasing and also can be used for filtration purposes such as air or water purification.

Figure 1b,c depicts the scanning electron microscopy (SEM) and transmission electron microscopy (TEM) images of Pd-decorated CNFs after a 1 s and 5 ms thermal shock at  $\sim 2000$  K. A large number of Pd nanoparticles were formed and uniformly distributed along the CNFs. The average size of Pd nanoparticles formed by the 5 ms shock ( $\sim 4$  nm) is much smaller compared to the 1 s shock ( $\sim 27$  nm), demonstrating the temporal confinement of shock time on the synthesis of ultrafine NPs. The corresponding SEM images of CNF and CNF- $\text{PdCl}_2$  can be found in Figure S1.

The rapid thermal shock process was triggered by electrical Joule heating, and its temperature was controlled by the input electrical power.<sup>37–43</sup> The carbon-based samples were attached to copper electrodes, placed in an argon environment, and connected to an external current source (Keithley 2400). Figure 2a shows images of the CNF- $\text{PdCl}_2$  ( $3$  mm  $\times$   $1$  mm  $\times$   $30$   $\mu\text{m}$ ) before and during the thermal shock process. In this example, a 1 s 100 mA current (or 1.54 W) pulse was applied to the sample whose temperature was raised up quickly due to direct Joule heating. Carbon materials at high temperatures will emit bright light as a radiation source due to gray-body radiation, and the spectrum can be used for temperature evaluation according to black-body theory. The emission spectrum was collected by an optical fiber (400  $\mu\text{m}$ , ocean optics) and dispersed using a spectrometer (Ocean Optics USB 2000+).

Figure 2b depicts the temporal evolution of emitted light intensity during the rapid high temperature process at 800 nm, and overlaid with the 100 mA pulse. The emission intensity induced by the 100 mA pulse saturated within 0.1 s, equilibrated, and subsequently dropped after the pulse ended. Both an ultrafast heating and cooling rate were achieved during the thermal shock process, owing to the direct Joule heating,

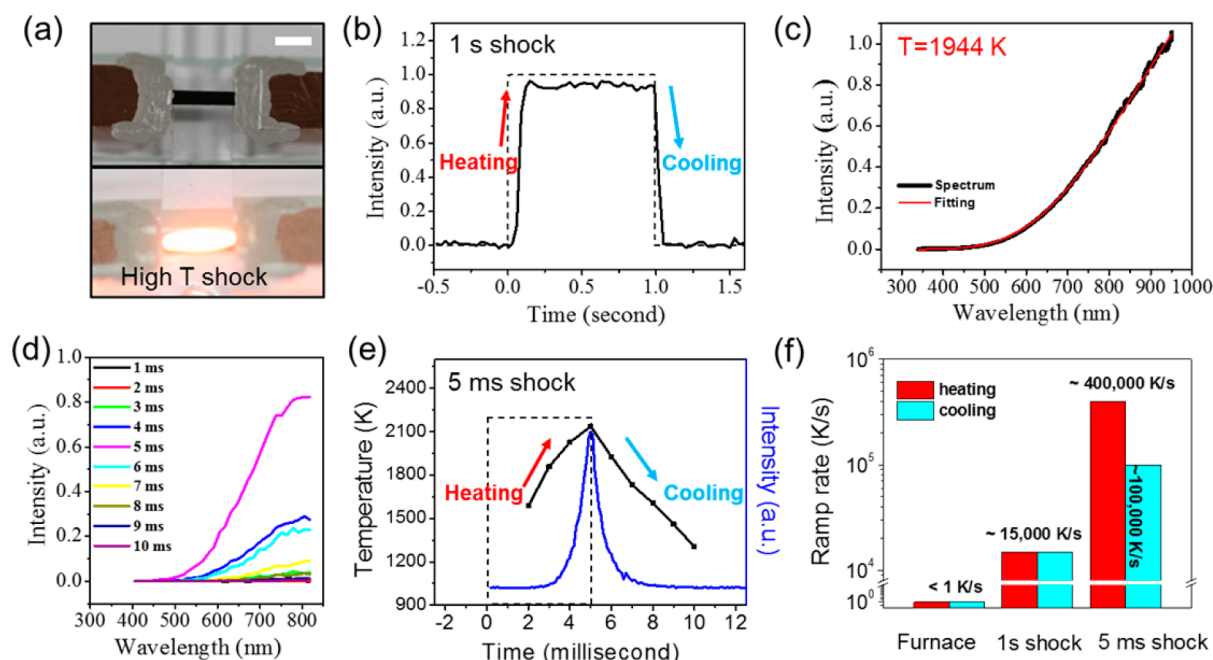


**Figure 2.** Characterization of the rapid high temperature thermal shock method. (a) Digital images of the CNF-PdCl<sub>2</sub> sample before and during thermal shock. Scale bar: 2 mm. (b) Evolution of light emission intensity during the 1 s thermal shock treatment with a 100 mA current pulse. (c) Emitted light spectrum for the 1 s shock at 100 mA. The spectra are fitted to the gray-body radiation model using a temperature of 1944 K. (d) Light emission spectra at different times from 0 to 10 ms, covering both the heating and cooling of 5 ms thermal shock at 100 mA. (e) The temporal evolution of temperature and light intensity at 800 nm for the 5 ms thermal shock. (f) Temperature ramp rate for conventional furnace heating, 1 s thermal shock, and 5 ms thermal shock.

the good thermal conductivity of carbon materials, and also small sample size. The full spectrum from 350 to 950 nm was collected and fitted to the gray-body radiation equation to determine the sample temperature during thermal shock (Figure 2c).<sup>42–44</sup> Although carbon materials are not exactly a black-body source, they have a stable emissivity around 0.8 for the measured wavelength range to ensure the fitting accuracy.<sup>37</sup> In this 1 s shock process, the estimated temperature was approximately 1950 K, which confirms that the temperature induced by the thermal shock method was more than enough for PdCl<sub>2</sub> decomposition.

The exceptional temperature control via Joule heating can be further illustrated by an ultrafast 5 ms thermal shock duration (Figure 2d,e). The rapid thermal shock held for 5 ms is beyond the temporal resolution of commercial spectrometers. Thus, a specially designed spectrometer, capable of sub-millisecond diagnostics with a temporal resolution down to 2.5 μs, was used to monitor the thermal shock pulse as shown in Figure 2d. Both the electrical pulse and above spectrometer were triggered at the same time for the measurement. Despite the thermal shock duration's being 5 ms, the emitted light was monitored from 0 to 20 ms to cover both the heating and subsequent cooling period. These spectra at different times during the shock were fitted to the gray-body radiation equation to extract the temperature vs time profiles (Figure 2e). As the spectrometer cannot properly detect below 1000 K, the temporal light emission at 800 nm was overlapped with the temperature evolution curve to illustrate the heating and cooling process. To heat from room temperature to the peak temperature of 2100 K takes a mere 5 ms, which roughly translates to a ramp rate of 400,000 K/s.

Figure 2f summarizes and compares the ramp rates of the proposed thermal shock method to conventional heating in a

furnace. For furnace-based heating, the heating/cooling ramp rate is limited to 10 K/min (<1 K/s) due to slow radiation heating and an expansive heating volume. For electrically triggered Joule heating via thermal shock, the temperature increases by direct Joule heating effects and the size of the sample is orders of magnitude smaller than a conventional furnace chamber size. This enables the ramp rate for the proposed thermal shock method to be exceptionally large. For a 1 s thermal shock, the heating and cooling processes occurred within 100–130 ms (Figure 2b), which corresponds to a heating/cooling rate of ~15,000 K/s. For the 5 ms thermal shock, a 400,000 K/s heating rate was demonstrated (Figure 2e). Since initial cooling from 2100 to 1200 K takes only 5 ms (180,000 K/s), the cooling rate was roughly estimated to be ~100,000 K/s for a total cooling time of 20 ms. Thus, the exceptional ramp rates of the Joule heating process and the ability to tune the thermal pulse time provide extreme kinetic control for the synthesis of nanoparticles.

Besides the formation of NPs on the CNFs, we also investigated the impact of the thermal shock method on the CNF substrate, and data is included in Figure S2. Although the high temperature achieved by the thermal shock process is much higher than the CNF carbonization temperature (600 °C), the thermal shock pulse is not detrimental to the substrate due to its short duration and the inert atmosphere during the application of the shock pulse. This is confirmed with Raman and XRD analysis that show no change before and after the thermal shock method. In contrast, our CNFs under extended pulse time (100 s) at high temperature carbonize the fibers further and result in substantial changes in both the Raman and XRD spectra. Therefore, a short thermal shock duration causes the sample to reach high enough temperatures to induce thermal decomposition with minimal impact to the substrate

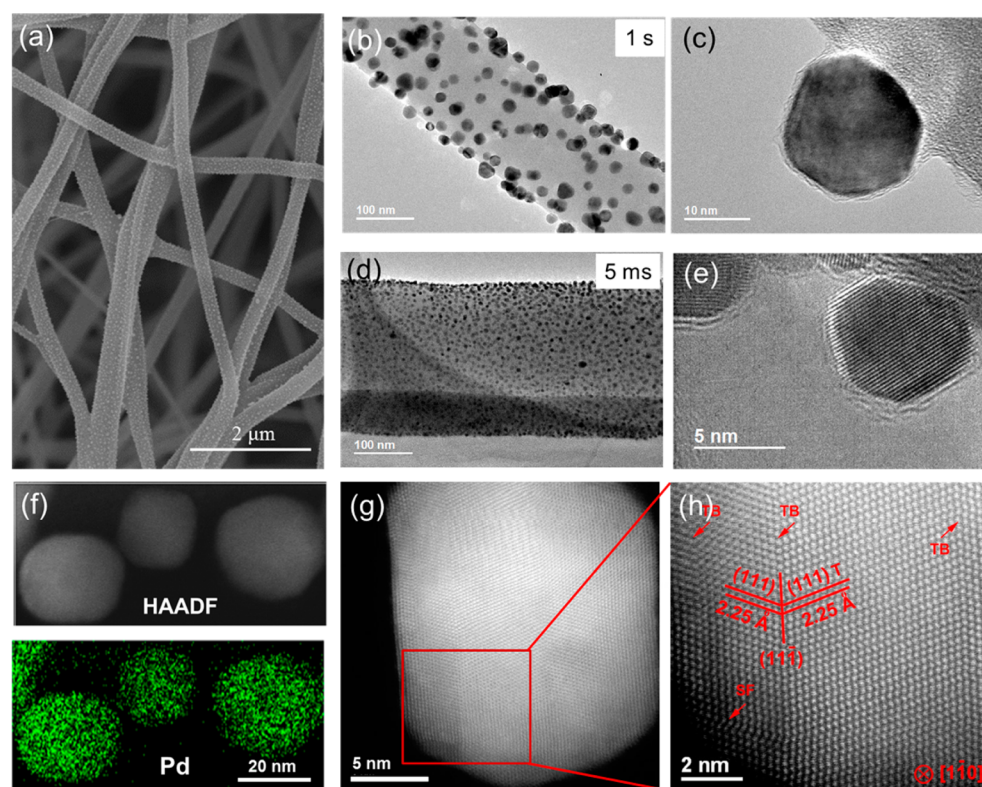


**Figure 3.** Microstructure of Pd/CNFs using the rapid thermal shock method. (a) SEM image and (b, c) TEM images of Pd nanoparticles formed on CNFs by a 1 s thermal shock treatment. (d, e) TEM images of Pd nanoparticles formed on CNF by a 5 ms thermal shock treatment. (f) HAADF-STEM image and EDX elemental map of the Pd/CNF sample fabricated with a 1 s thermal shock. (g, h) Atomic-scale HAADF-STEM image of a Pd nanoparticle formed on CNF surface along the  $[1\bar{1}0]$  zone axis. Twin boundaries (TBs) and stacking faults (SFs) are present due to the nonequilibrium rapid thermal shock.

(i.e., CNFs). Substrates typically cannot withstand the (high) temperatures of conventional processing techniques, which demonstrates the unique potential of the proposed high temperature synthesis method.

The microstructure of the *in situ* synthesized Pd nanoparticles on the CNF matrix was examined by SEM and TEM. Based on the thermal pulse duration, the proposed rapid thermal shock method creates nanoparticles with specific sizes and distributions. After a 1 s thermal shock at 100 mA, Pd nanoparticles are uniformly distributed across the entire CNF sample (Figure 3a). The formation of metallic Pd nanoparticles from  $\text{PdCl}_2$  by thermal decomposition was confirmed by X-ray photoelectron spectroscopy (XPS) (Figure S3), showing the metallic Pd 3d peak. Figure 3b,c are TEM images of the aforementioned Pd nanoparticles with an average size of approximately 27 nm. The as formed Pd nanoparticles are anchored to the CNF surface, ensuring the maximum exposure of NPs as contrast with NPs buried inside the carbon matrix.<sup>45,24,9,5,10</sup> The attached Pd nanoparticles were firmly anchored onto the CNF surface, which was verified by sonicating the TEM samples for several hours in ethanol before imaging the well-preserved NPs. Figure 3d,e exhibits Pd nanoparticles on CNF using a 100 mA pulse for 5 ms. Using a short thermal shock duration, the average Pd NP size is approximately 4 nm. This verifies the proposed mechanism where an extremely short shock duration enables the synthesis of smaller nanoparticles due to temporal limitations on mass diffusion and migration. The synthesized Pd NPs possess a highly crystalline structure as shown in the high-resolution TEM image (Figure 3e). Thus, the rapid thermal shock method

can fabricate high purity nanoparticles on carbon-based materials in a facile manner.

Figure 3f shows a typical low magnification high angle annular dark field scanning TEM (HAADF-STEM) image of the synthesized Pd nanoparticles on CNFs using a 1 s thermal shock. Since the intensity of the HAADF-STEM image is proportional to the atomic number  $Z^{1.7}$  of the sample,<sup>46</sup> the CNF matrix appears dark, however, the Pd nanoparticles can be easily identified. The energy dispersive X-ray mapping (EDX) illustrates the elemental distribution of Pd on the sample. The Pd mapping coincides with the nanoparticles on the CNF surface, which confirms the chemical composition of the synthesized nanoparticles. In order to obtain more detailed structural information on the synthesized Pd nanoparticles, atomic-scale HAADF-STEM was employed (Figure 3g,h). The atomic-scale HAADF-STEM image coincided with the  $[1\bar{1}0]$  zone axis of the Pd nanoparticle since the  $d$ -spacing of the main lattice planes matches well with the (111) and  $(1\bar{1}\bar{1})$  planes of the fcc Pd metal ( $Fm\bar{3}m$ ,  $a = b = c = 3.867$ , JPCDF 87-0645). Notably, this Pd nanoparticle contains several twin boundaries (TBs) and stacking faults (SFs) along the  $\{111\}$  planes, which are marked by red arrows in Figure 3h. The existence of TBs and SFs in the Pd nanoparticles may have an effect on the electrocatalytic activity of the Pd/CNFs. More specifically, these planar defects are favorable in chemical reactions<sup>47</sup> and ionic diffusion<sup>48</sup> due to their high lattice energy.

In wet chemistry, Pd seeds or nanoparticles with sizes smaller than 10 nm form twin boundaries and thus icosahedral or dodecahedral structures to minimize the surface energy, which has been proven by both experimental and simulated

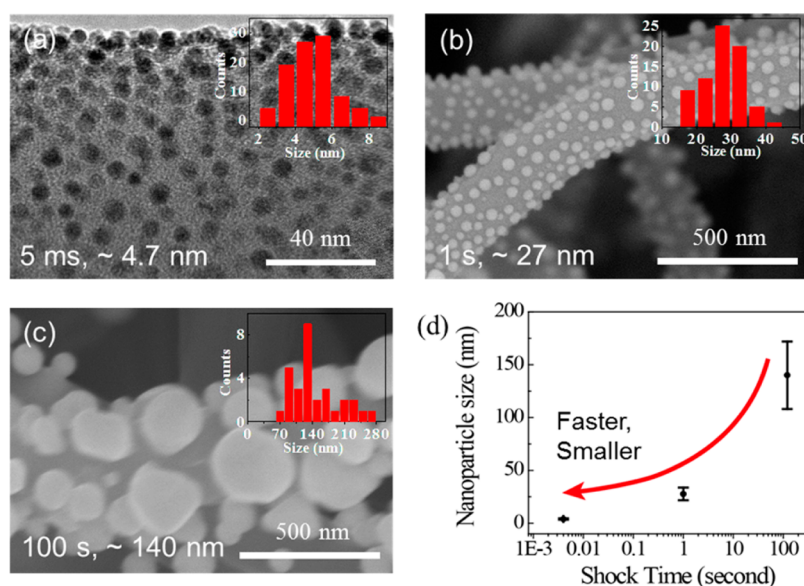


**Figure 4.** Kinetic variations on the formation of Pd/CNFs. (a) TEM and (b, c) SEM images of the Pd/CNFs formed with a 100 mA thermal shock for 5 ms, 1 s, and 100 s, respectively. Insets are histograms of the particle size distribution for each thermal shock condition. (d) Average nanoparticle size as a function of shock duration time. As the thermal shock time decreases, the nanoparticle size becomes smaller with a more uniform distribution. Scale bar: standard deviation.

results.<sup>49–52</sup> Owing to the anisotropy in Pd crystal structures, the thermodynamically favorable forms are multiple twinned {111} structures. The synthesis of NPs by wet chemistry is near thermodynamic equilibrium and is achieved by controlling the reduction and growth rate of Pd atoms for selective facet growth. Such a slow reduction limits the concentration of Pd atoms and promotes the formation of thermodynamically favored twinned seeds, which can later evolve into icosahedral or dodecahedral structures. However, the nanoparticles synthesized by rapid thermal shock form disordered twin boundaries (TBs) and stacking faults (SFs) despite the high stacking fault energy of Pd (Figure 3h and Figure S4). The formation of such disordered TBs and SFs in large Pd nanoparticles may arise from the nonequilibrium synthesis process that occurs with the rapid thermal shock method. The ultrafast cooling rate could induce and lock SFs and TBs within the Pd nanoparticles to create the nonequilibrium metastable structure. In the rapid thermal shock case, Pd NPs are formed through ultrafast thermal reduction of PdCl<sub>2</sub> into Pd atoms, where a huge amount of Pd atoms were reduced in milliseconds. Such an ultrafast thermal reduction gives an overwhelming amount of Pd atoms that will aggregate quickly and nucleate into nanoparticles during the rapid cooling process. In this case, the Pd atoms do not have enough time for the equilibrium growth and crystallization into well-ordered crystal structures and, therefore, form high concentrations of disordered TBs and SFs during the rapid condensation process.

The catalytic properties of the synthesized Pd/CNFs were also evaluated (Figure S5). A CNF matrix uniformly loaded with Pd nanoparticles is an ideal structure for electrical catalysis, specifically fuel cells, lithium–oxygen batteries, and flow catalysis, among others.<sup>13,53–55</sup> The porous CNF matrix provides a conductive support structure for Pd nanoparticles while facilitating gases/solutions to flow throughout the structure for catalysis. In this work, we demonstrate the aforementioned Pd/CNFs for the favorable catalytic decomposition of methylene blue.

To evaluate the dependence of nanoparticle size and distribution on the high temperature thermal shock conditions, the Joule heating time and temperature were varied. Figure 4a–c exhibits SEM images of the Pd/CNFs formed with a 100 mA Joule heating over various shock durations (5 ms, 1 s, and 100 s). By altering the duration time of the high temperature synthesis, the average nanoparticle size and distribution change dramatically, where shorter thermal shock times lead to smaller nanoparticle sizes with narrower size distributions. More specifically, for the 1 s and 5 ms shock, the average nanoparticle size changed from 27.7 to 4.2 nm with a size distribution ranging between 4.5 and 0.5 nm, respectively. In contrast to the rapid thermal shock method, Figure 4c shows the SEM image of Pd/CNF subjected to 100 s of high temperature heating. The resultant Pd nanoparticles have a broad size distribution with a much larger particle size (~140 nm) than the rapid thermal shock durations (5 ms and 1 s). Additionally, by 100 s of high temperature heating, some CNF areas were not loaded with Pd particles while others suffered from aggregation. This indicates that severe nanoparticle migration occurs with prolonged high temperature heating.

Figure 4d summarizes the average size of the Pd nanoparticles as a function of thermal shock time. It is clear that the size distribution is dominantly affected by thermal shock time as a temporal constraint in the NP synthesis: the faster thermal shock can lead to smaller size nanoparticles with narrower size distribution. The rapid thermal shock temperatures were also varied by tuning the applied current pulse (100 mA, 50 mA, and 20 mA) (Figure S6). Based on the temperature vs applied current plot (Figure S7), the thermal shock conditions for 100 mA, 50 mA, and 20 mA correspond to temperatures of 2000 K, 1700 K, and 1300 K, respectively. As the thermal shock changed from 100 mA to 50 mA, and to 20 mA, the average size changed subtly from 27 nm to 21 nm, and to 19.7 nm. Therefore, compared to the size dependence on shock time, the dependence of nanoparticle size on shock temperature is much weaker.

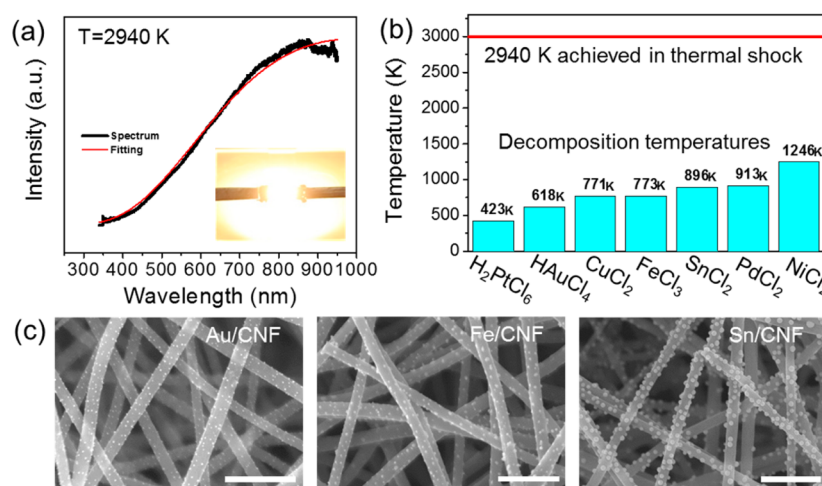


**Figure 5.** Rapid thermal shock as a universal NP synthesis method. (a) A plot demonstrating the high temperature ( $\sim 3000$  K) achieved by Joule heating. The inset is a digital image of the sample during the high temperature process. (b) Thermal decomposition temperatures of metal (chloride-based) precursor salts. (c) Synthesis of NP/CNFs (Au, Fe, Sn) by thermal shock at 2000 K. Scale bar:  $1 \mu\text{m}$ .

Since the thermal decomposition of metal salts is a universal reaction mechanism, the synthesis of NPs with the proposed rapid thermal shock method can be easily extended to numerous other metals. By electrical Joule heating, the temperature of the thermal shock can reach  $\sim 3000$  K (Figure 5a). The high temperature achieved by the thermal shock method is high enough to decompose most metal salts, such as platinum (Pt), gold (Au), iron (Fe), tin (Sn), and nickel (Ni), among others.<sup>56</sup> Figure 5b exhibits a selected number of metal salt decomposition temperatures compared to the peak thermal shock temperature of the proposed high temperature synthesis method. Similar to the synthesis of Pd nanoparticles, when the metal salts are exposed to the sufficiently high thermal shock temperature for a short duration of time, metal nanoparticles can readily form. Au-, Fe-, and Sn-based CNF samples were Joule heated to  $\sim 2000$  K for 1 s to enable the *in situ* synthesis of uniformly distributed nanoparticles on the CNF surface. Figure 5c exhibits the synthesized NP/CNF (Au, Fe, Sn) samples to demonstrate the universality of the proposed high temperature thermal shock method.

In summary, we report a universal high temperature method for *in situ* synthesis of nanoparticles on a carbon fiber matrix using metal precursor salts. This high temperature thermal shock method can be used for a range of applications such as water treatment, energy storage, and electrochemical water splitting. With Pd nanoparticle as the model system in the study, we thoroughly investigated the temporal distribution of temperatures with high-resolution spectrometer down to milliseconds. The typical ramp rates are  $\sim 400,000$  K/s for heating and  $\sim 100,000$  K/s for cooling, which are orders of magnitude higher than values reported in the literature for other NP synthesis, and are crucial for achieving smaller nanoparticles with a more uniform size distribution. We extended the high temperature thermal shock method to the synthesis of other nanoparticles including Au, Fe, and Sn, suggesting that the method can be applied for the synthesis of a wide range of other nanoparticles with salt decomposition temperatures less than  $\sim 3000$  K.

## METHODS

**Preparation of CNF with Metal Salts.** CNFs were prepared by electrospinning polyacrylonitrile (PAN) (Sigma-

Aldrich) with a concentration of 8 wt % in dimethylformamide (DMF) at a voltage of 10 kV (spinning distance of 15 cm; rate of 1 mL/h). The as-spun nanofibers were collected by a rotation drum at a speed of 80 rpm. The nanofiber mat was then stabilized at  $260^\circ\text{C}$  for 5 h in air and carbonized at  $600^\circ\text{C}$  in an argon atmosphere for 2 h to obtain the CNFs. The CNF film was then dipped in a 1 mg/mL  $\text{PdCl}_2$  solution (with vacuum assistance) and dried in an oven. The as-prepared CNF- $\text{PdCl}_2$  film was used directly for high temperature thermal shock experiments.

**Rapid Thermal Shock Synthesis.** Rapid thermal shock was realized by electrical Joule heating in an argon-filled glovebox. The CNF- $\text{PdCl}_2$  film was connected to copper electrodes, and the interfaces were glued together with silver paste. The external current source was supplied by a Keithley 2400 SourceMeter. When the sample was exposed to high temperature, the emitted light was collected by an optical fiber and sent to a spectrometer (Ocean Optics). The measurement system was calibrated by a National Institute of Standards and Technology (NIST) traceable light source. For ultrafast thermal shock of 5 ms, which is beyond the resolution capability of optical fiber, we used a specifically designed online pyrometer with a 1200 groove/mm grating that can disperse the light at a spatial resolution down to 0.8 nm/mm. The dispersed light was then collected by a 32-channel PMT array to form the full spectrum, with a temporal resolution down to 2.5  $\mu\text{s}$ .

**Characterization.** The microstructure and morphology of the prepared samples was observed with a Hitachi SU-70 FEG-SEM at 10 kV, a JEOL 2100 LaB<sub>6</sub> TEM operated at 200 kV, and a JEOL TEM/STEM FEG also operated at 200 kV. A 22 mrad probe convergence angle was used to perform STEM imaging. HAADF detector in the JEOL 2100 FEG TEM with 90 mrad inner-detector angle was utilized to obtain the Z-contrast atomic resolution images. For EDS data collection, an Oxford X-max 100TLE windowless X-ray detector was utilized. The average particle size and distribution were determined by ImageJ software using at least three microscopy images per sample. Raman measurements were performed with a Labram Aramis model by Horiba Jobin-Yvon using a 532 nm laser and an integration time of 4 s, which was repeated at least four times per sample. XPS analysis was performed on a Kratos Axis

165 X-ray photoelectron spectrometer. XRD data was collected by a D8 Advanced (Bruker AXS, Fitchburg, WI, USA).

## ■ ASSOCIATED CONTENT

### ● Supporting Information

The Supporting Information is available free of charge on the ACS Publications website at DOI: 10.1021/acscentsci.6b00374.

Microstructure, Raman spectra, XRD and XPS analysis, catalytic properties of Pd/CNF, temperature dependence of NP size, and the power–temperature relationship by Joule heating of CNF (PDF)

## ■ AUTHOR INFORMATION

### Corresponding Author

\*E-mail: [binghu@umd.edu](mailto:binghu@umd.edu).

### ORCID

Anmin Nie: 0000-0002-0180-1366

Michael R. Zachariah: 0000-0002-4115-3324

Reza Shahbazian-Yassar: 0000-0002-7744-4780

Liangbing Hu: 0000-0002-9456-9315

### Author Contributions

<sup>‡</sup>Y.Y. and F.C. contributed equally.

### Notes

The authors declare no competing financial interest.

## ■ ACKNOWLEDGMENTS

This project is supported by the NSF Scalable Nano-manufacturing Project No. 1635221. M.R.Z. and R.J.J. were also partially supported by an ONR-MURI grant. R.S.-Y. acknowledges the financial support from the National Science Foundation (Award No. CMMI-1619743). F.C. would like to acknowledge the National Natural Science Foundation of China (21401091) and the China Scholarship Council (CSC) for financial support. We would like to thank Dr. Karen Gaskell for the XPS data acquisition and analysis as well as Dr. Yuhuang Wang and Brendan Meany for the UV–vis measurements. The Maryland Nanocenter and its AIM Lab are also acknowledged for use of their microscopy facilities. The authors acknowledge the helpful discussions Sha Wang, Tingting Gao, and Hua Xie.

## ■ REFERENCES

- (1) Wang, D.; Zhu, L.; Chen, J. F.; Dai, L. Liquid Marbles Based on Magnetic Upconversion Nanoparticles as Magnetically and Optically Responsive Miniature Reactors for Photocatalysis and Photodynamic Therapy. *Angew. Chem., Int. Ed.* **2016**, *55*, 10795–10799.
- (2) Luo, Z.; Tan, C.; Zhang, X.; Chen, J.; Cao, X.; Li, B.; Zong, Y.; Huang, L.; Huang, X.; Wang, L.; et al. Preparation of Cobalt Sulfide Nanoparticle-Decorated Nitrogen and Sulfur Co-Doped Reduced Graphene Oxide Aerogel Used as a Highly Efficient Electrocatalyst for Oxygen Reduction Reaction. *Small* **2016**, *12*, 5920–5926.
- (3) Li, W.; Sheehan, S. W.; He, D.; He, Y.; Yao, X.; Grimm, R. L.; Brudvig, G. W.; Wang, D. Hematite-Based Solar Water Splitting in Acidic Solutions: Functionalization by Mono- and Multilayers of Iridium Oxygen-Evolution Catalysts. *Angew. Chem., Int. Ed.* **2015**, *54*, 11428–11432.
- (4) Zhang, L.; Roling, L. T.; Wang, X.; Vara, M.; Chi, M.; Liu, J.; Choi, S.-I.; Park, J.; Herron, J. A.; Xie, Z.; et al. Platinum-Based Nanocages with Subnanometer-Thick Walls and Well-Defined, Controllable Facets. *Science* **2015**, *349*, 412–416.
- (5) Prieto, G.; Zečević, J.; Friedrich, H.; de Jong, K. P.; de Jongh, P. E. Towards Stable Catalysts by Controlling Collective Properties of Supported Metal Nanoparticles. *Nat. Mater.* **2013**, *12*, 34–39.
- (6) Fu, K.; Yao, Y.; Dai, J.; Hu, L. Progress in 3D Printing of Carbon Materials for Energy-Related Applications. *Adv. Mater.* **2017**, *29*, 1603486.
- (7) Eggenhuisen, T. M.; de Jongh, P. E. Supported Nanoparticles. In *Nanoparticles*, de Mello Donega, C., Ed.; Springer-Verlag: Berlin Heidelberg, 2014; pp 121–127.
- (8) Corma, A.; Garcia, H. Supported Gold Nanoparticles as Catalysts for Organic Reactions. *Chem. Soc. Rev.* **2008**, *37*, 2096–2126.
- (9) Mayavan, S.; Jang, H.-S.; Lee, M.-J.; Choi, S. H.; Choi, S.-M. Enhancing the Catalytic Activity of Pt Nanoparticles Using Poly Sodium Styrene Sulfonate Stabilized Graphene Supports for Methanol Oxidation. *J. Mater. Chem. A* **2013**, *1*, 3489–3494.
- (10) He, D.; Cheng, K.; Peng, T.; Pan, M.; Mu, S. Graphene/carbon Nanospheres Sandwich Supported PEM Fuel Cell Metal Nanocatalysts with Remarkably High Activity and Stability. *J. Mater. Chem. A* **2013**, *1*, 2126–2132.
- (11) Liu, G.; Eichelsdoerfer, D. J.; Rasin, B.; Zhou, Y.; Brown, K. A.; Liao, X.; Mirkin, C. A. Delineating the Pathways for the Site-Directed Synthesis of Individual Nanoparticles on Surfaces. *Proc. Natl. Acad. Sci. U. S. A.* **2013**, *110*, 887–891.
- (12) Alvarado, S. R.; Guo, Y.; Ruberu, T. P. A.; Bakac, A.; Vela, J. Photochemical versus Thermal Synthesis of Cobalt Oxyhydroxide Nanocrystals. *J. Phys. Chem. C* **2012**, *116*, 10382–10389.
- (13) Zhang, P.; Shao, C.; Zhang, Z.; Zhang, M.; Mu, J.; Guo, Z.; Liu, Y. In Situ Assembly of Well-Dispersed Ag Nanoparticles (AgNPs) on Electrospun Carbon Nanofibers (CNFs) for Catalytic Reduction of 4-Nitrophenol. *Nanoscale* **2011**, *3*, 3357–3363.
- (14) Chen, X.; Wu, G.; Chen, J.; Chen, X.; Xie, Z.; Wang, X. Synthesis Of “clean” and Well-Dispersive Pd Nanoparticles with Excellent Electrocatalytic Property on Graphene Oxide. *J. Am. Chem. Soc.* **2011**, *133*, 3693–3695.
- (15) McGilvray, K. L.; Decan, M. R.; Wang, D.; Scaiano, J. C. Facile Photochemical Synthesis of Unprotected Aqueous Gold Nanoparticles. *J. Am. Chem. Soc.* **2006**, *128*, 15980–15981.
- (16) Fu, G.; Tao, L.; Zhang, M.; Chen, Y.; Tang, Y.; Lin, J.; Lu, T. One-Pot, Water-Based and High-Yield Synthesis of Tetrahedral Palladium Nanocrystal Decorated Graphene. *Nanoscale* **2013**, *5*, 8007–8014.
- (17) Pang, X.; He, Y.; Jung, J.; Lin, Z. 1D Nanocrystals with Precisely Controlled Dimensions, Compositions, and Architectures. *Science (Washington, DC, U. S.)* **2016**, *353*, 1268–1272.
- (18) Gilroy, K. D.; Ruditskiy, A.; Peng, H.-C.; Qin, D.; Xia, Y. Bimetallic Nanocrystals: Syntheses, Properties, and Applications. *Chem. Rev.* **2016**, *116*, 10414–10472.
- (19) Fan, Z.; Zhang, H. Crystal Phase-Controlled Synthesis, Properties and Applications of Noble Metal Nanomaterials. *Chem. Soc. Rev.* **2016**, *45*, 63–82.
- (20) Chen, A.; Ostrom, C. Palladium-Based Nanomaterials: Synthesis and Electrochemical Applications. *Chem. Rev.* **2015**, *115*, 11999–12044.
- (21) Chen, H.; Wang, D.; Yu, Y.; Newton, K. A.; Muller, D. A.; Abruña, H.; Disalvo, F. J. A Surfactant-Free Strategy for Synthesizing and Processing Intermetallic Platinum-Based Nanoparticle Catalysts. *J. Am. Chem. Soc.* **2012**, *134*, 18453–18459.
- (22) Ganguli, A. K.; Ganguly, A.; Vaidya, S. Microemulsion-Based Synthesis of Nanocrystalline Materials. *Chem. Soc. Rev.* **2010**, *39*, 474–485.
- (23) Amendola, V.; Meneghetti, M. Laser Ablation Synthesis in Solution and Size Manipulation of Noble Metal Nanoparticles. *Phys. Chem. Chem. Phys.* **2009**, *11*, 3805–3821.
- (24) Jin, Z.; Nackashi, D.; Lu, W.; Kittrell, C.; Tour, J. M. Decoration, Migration, and Aggregation of Palladium Nanoparticles on Graphene Sheets. *Chem. Mater.* **2010**, *22*, 5695–5699.
- (25) Gao, Y.; Bando, Y. Carbon Nanothermometer Containing Gallium. *Nature* **2002**, *415*, 599–599.
- (26) Gao, Y. H.; Sun, M.; Su, J.; Zhi, C. Y.; Golberg, D.; Bando, Y.; Duan, X. F. Electron-Beam Induced Electric-Hydraulic Expansion in a Silica-Shelled Gallium Microball-Nanotube Structure. *Appl. Phys. Lett.* **2011**, *99*, 083112.

- (27) Chen, Y.; Huang, Y.; Liu, N.; Su, J.; Li, L.; Gao, Y. Fabrication of Nanoscale Ga Balls via a Coulomb Explosion of Microscale Silica-Covered Ga Balls by TEM Electron-Beam Irradiation. *Sci. Rep.* **2015**, *5*, 11313.
- (28) Park, I.; Li, Z. Y.; Pisano, A. P.; Williams, R. S. Selective Surface Functionalization of Silicon Nanowires via Nanoscale Joule Heating. *Nano Lett.* **2007**, *7*, 3106–3111.
- (29) Barbangelo, A.; Sangiorgi, R. Wetting Properties of Metal/Carbon Systems. In *Wettability at High Temperatures*; Eustathopoulos, N., Nicholas, M. G., Drevet, B., Eds.; Pergamon: 1999; Vol. 3, pp 317–338.
- (30) Stern, L.-A.; Feng, L.; Song, F.; Hu, X. Ni<sub>2</sub>P as a Janus Catalyst for Water Splitting: The Oxygen Evolution Activity of Ni<sub>2</sub>P Nanoparticles. *Energy Environ. Sci.* **2015**, *8*, 2347–2351.
- (31) Wang, T.; Wang, H.; Chi, X.; Li, R.; Wang, J. Synthesis and Microwave Absorption Properties of Fe-C Nanofibers by Electrospinning with Disperse Fe Nanoparticles Parceled by Carbon. *Carbon* **2014**, *74*, 312–318.
- (32) Li, W. C.; Comotti, M.; Schüth, F. Highly Reproducible Syntheses of Active Au/TiO<sub>2</sub> Catalysts for CO Oxidation by Deposition-Precipitation or Impregnation. *J. Catal.* **2006**, *237*, 190–196.
- (33) Xue, Y.; Chen, H.; Yu, D.; Wang, S.; Yardeni, M.; Dai, Q.; Guo, M.; Liu, Y.; Lu, F.; Qu, J.; et al. Oxidizing Metal Ions with Graphene Oxide: The in Situ Formation of Magnetic Nanoparticles on Self-Reduced Graphene Sheets for Multifunctional Applications. *Chem. Commun.* **2011**, *47*, 11689–11691.
- (34) Deng, J.; Kang, L.; Bai, G.; Li, Y.; Li, P.; Liu, X.; Yang, Y.; Gao, F.; Liang, W. Solution Combustion Synthesis of Cobalt Oxides (Co<sub>3</sub>O<sub>4</sub> and Co<sub>3</sub>O<sub>4</sub>/CoO) Nanoparticles as Supercapacitor Electrode Materials. *Electrochim. Acta* **2014**, *132*, 127–135.
- (35) Manikandan, A.; Vijaya, J. J.; Mary, J. A.; Kennedy, L. J.; Dinesh, A. Structural, Optical and Magnetic Properties of Fe<sub>3</sub>O<sub>4</sub> Nanoparticles Prepared by a Facile Microwave Combustion Method. *J. Ind. Eng. Chem.* **2014**, *20*, 2077–2085.
- (36) Guo, J.; Liu, Q.; Wang, C.; Zachariah, M. R. Interdispersed Amorphous MnOx–Carbon Nanocomposites with Superior Electrochemical Performance as Lithium-Storage Material. *Adv. Funct. Mater.* **2012**, *22*, 803–811.
- (37) Bao, W.; Pickel, A. D.; Zhang, Q.; Chen, Y.; Yao, Y.; Wan, J.; Fu, K.; Wang, Y.; Dai, J.; Zhu, H.; et al. Flexible, High Temperature, Planar Lighting with Large Scale Printable Nanocarbon Paper. *Adv. Mater.* **2016**, *28*, 4684–4691.
- (38) Chen, Y.; Egan, G. C.; Wan, J.; Zhu, S.; Jacob, R. J.; Zhou, W.; Dai, J.; Wang, Y.; Danner, V. A.; Yao, Y.; et al. Ultra-Fast Self-Assembly and Stabilization of Reactive Nanoparticles in Reduced Graphene Oxide Films. *Nat. Commun.* **2016**, *7*, 12332.
- (39) Chen, Y.; Li, Y.; Wang, Y.; Fu, K.; Danner, V. A.; Dai, J.; Lacey, S. D.; Yao, Y.; Hu, L. Rapid, in Situ Synthesis of High Capacity Battery Anodes through High Temperature Radiation-Based Thermal Shock. *Nano Lett.* **2016**, *16*, 5553–5558.
- (40) Kim, Y. D.; Kim, H.; Cho, Y.; Ryoo, J. H.; Park, C.-H.; Kim, P.; Kim, Y. S.; Lee, S.; Li, Y.; Park, S.-N.; et al. Bright Visible Light Emission from Graphene. *Nat. Nanotechnol.* **2015**, *10*, 676–681.
- (41) Mann, D.; Kato, Y. K.; Kinkhabwala, A.; Pop, E.; Cao, J.; Wang, X.; Zhang, L.; Wang, Q.; Guo, J.; Dai, H. Electrically Driven Thermal Light Emission from Individual Single-Walled Carbon Nanotubes. *Nat. Nanotechnol.* **2007**, *2*, 33–38.
- (42) Yao, Y.; Fu, K. K.; Yan, C.; Dai, J.; Chen, Y.; Wang, Y.; Zhang, B.; Hitz, E.; Hu, L. Three-Dimensional Printable High-Temperature and High-Rate Heaters. *ACS Nano* **2016**, *10*, 5272–5279.
- (43) Yao, Y.; Fu, K. K.; Zhu, S.; Dai, J.; Wang, Y.; Pastel, G.; Chen, Y.; Li, T.; Wang, C.; Li, T.; et al. Carbon Welding by Ultrafast Joule Heating. *Nano Lett.* **2016**, *16*, 7282–7289.
- (44) Neuer, G. Spectral and Total Emissivity Measurements of Highly Emitting Materials. *Int. J. Thermophys.* **1995**, *16*, 257–265.
- (45) Sun, X.; Li, Y. Colloidal Carbon Spheres and Their Core/Shell Structures with Noble-Metal Nanoparticles. *Angew. Chem., Int. Ed.* **2004**, *43*, 597–601.
- (46) Pennycook, S. J. Structure Determination through Z-Contrast Microscopy. *Adv. Imaging Electron Phys.* **2002**, *123*, 173–206.
- (47) Liu, M.; Wang, L.; Lu, G.; Yao, X.; Guo, L. Twins in Cd<sub>1-x</sub>ZnxS Solid Solution: Highly Efficient Photocatalyst for Hydrogen Generation from Water. *Energy Environ. Sci.* **2011**, *4*, 1372–1378.
- (48) Nie, A.; Gan, L.-Y.; Cheng, Y.; Li, Q.; Yuan, Y.; Mashayek, F.; Wang, H.; Klie, R.; Schwingschlogl, U.; Shahbazian-Yassar, R. Twin Boundary-Assisted Lithium Ion Transport. *Nano Lett.* **2015**, *15*, 610–615.
- (49) Baletto, F.; Ferrando, R.; Fortunelli, A.; Montalenti, F.; Mottet, C. Crossover among Structural Motifs in Transition and Noble-Metal Clusters. *J. Chem. Phys.* **2002**, *116*, 3856–3863.
- (50) Baletto, F.; Mottet, C.; Ferrando, R. Microscopic Mechanisms of the Growth of Metastable Silver Icosahedra. *Phys. Rev. B: Condens. Matter Mater. Phys.* **2001**, *63*, 155408.
- (51) Xiong, Y.; Xia, Y. Shape-Controlled Synthesis of Metal Nanostructures: The Case of Palladium. *Adv. Mater.* **2007**, *19*, 3385–3391.
- (52) Zhang, H.; Jin, M.; Xiong, Y.; Lim, B.; Xia, Y. Shape-Controlled Synthesis of Pd Nanocrystals and Their Catalytic Applications. *Acc. Chem. Res.* **2013**, *46*, 1783–1794.
- (53) Xu, Y.; Liu, Q.; Zhu, Y.; Liu, Y.; Langrock, A.; Zachariah, M. R.; Wang, C. Uniform Nano-Sn/C Composite Anodes for Lithium Ion Batteries. *Nano Lett.* **2013**, *13*, 470–474.
- (54) Chung, H. T.; Won, J. H.; Zelenay, P. Active and Stable Carbon Nanotube/nanoparticle Composite Electrocatalyst for Oxygen Reduction. *Nat. Commun.* **2013**, *4*, 1922.
- (55) Shen, Y.; Sun, D.; Yu, L.; Zhang, W.; Shang, Y.; Tang, H.; Wu, J.; Cao, A.; Huang, Y. A High-Capacity Lithium-Air Battery with Pd Modified Carbon Nanotube Sponge Cathode Working in Regular Air. *Carbon* **2013**, *62*, 288–295.
- (56) Galwey, A. K.; Brown, M. E. *Thermal Decomposition of Ionic Solids: Chemical Properties and Reactivities of Ionic Crystalline Phases*; Elsevier: New York, 1999; Vol. 86.